Environmental Fluid Mechanics **2:** 35–63, 2002.

Effects of the Resolution and Kinematics of Olfactory Appendages on the Interception of Chemical Signals in a Turbulent Odor Plume

J.P. CRIMALDI[a,*], M.A.R. KOEHL[b] and J.R. KOSEFF[c]
[a]*University of Colorado, Boulder, CO 80309-0428, U.S.A.*
[b]*University of California, Berkeley, CA 94720-3140, U.S.A.*
[c]*Stanford University, Stanford, CA 94305-4020, U.S.A.*

Received 17 August 2001; accepted in revised form 23 January 2002

Abstract. A variety of animals use olfactory appendages bearing arrays of chemosensory neurons to detect chemical signatures in the water or air around them. This study investigates how particular aspects of the design and behavior of such olfactory appendages on benthic aquatic animals affect the patterns of intercepted chemical signals in a turbulent odor plume. We use virtual olfactory 'sensors' and 'antennules' (arrays of sensors on olfactory appendages) to interrogate the concentration field from an experimental dataset of a scalar plume developing in a turbulent boundary layer. The aspects of the sensors that we vary are: (1) The spatial and temporal scales over which chemical signals arriving at the receptors of a sensor are averaged (e.g., by subsequent neural processing), and (2) the shape and orientation of a sensor with respect to ambient water flow. Our results indicate that changes in the spatial and temporal resolution of a sensor can dramatically alter its interception of the intermittency and variability of the scalar field in a plume. By comparing stationary antennules with those sweeping through the flow (as during antennule flicking by the spiny lobster, *Panulirus argus*), we show that flicking alters the frequency content of the scalar signal, and increases the likelihood that the antennule encounters peak events. Flicking also enables a long, slender (i.e., one-dimensional) antennule to intercept two-dimensional scalar patterns.

Key words: antennule, flicking, lobster, olfaction, plume, scalar structure, sensor, turbulence

1. Introduction

Many aquatic animals use chemical cues in the water around them to locate mates, food, or suitable habitats, and to detect competitors or predators. Not only are such activities ecologically important, but the mechanisms animals use to locate odor sources can provide insights for the design of artificial odor sensors and for the development of search algorithms. Turbulent water flow in the environment disperses odor molecules from a source, thus the spatial patterns of odor concentration in a turbulent plume can provide information that animals might use to locate the source of the smell. A number of recent studies have detailed the hydrodynamic and scalar structure of odor plumes for a wide range of flow conditions. Nonetheless,

*Corresponding author, E-mail: john.crimaldi@colorado.edu

the spatial and temporal scales at which animals sample such plumes is not yet understood.

For many types of organisms, such as crustaceans, the olfactory organs that capture odor molecules from the surrounding fluid are appendages (e.g., antennae, antennules) that are held in or flicked through ambient water currents. The purpose of the present study is to explore how certain aspects of the design and behavior of such olfactory organs affect the intermittency and variability of the chemical signals they intercept in a turbulent odor plume. We focus on bottom-dwelling ('benthic') animals exposed to an odor plume from a source on the substratum. The aspects of the design and behavior of olfactory antennules on which we focus are: (1) The spatial and temporal scales over which the chemical signals arriving at the receptors of an antennule are averaged (by subsequent neural processing), (2) the orientation of an olfactory organ with respect to ambient water flow, and (3) the flicking behavior of an antennule. We begin with a brief review of previous work on the structure of turbulent plumes and on the structure, behavior, and fluid dynamics of the olfactory antennules of crustaceans that have served as model systems for studying aquatic odor-plume tracking.

1.1. SPATIAL AND TEMPORAL STRUCTURE OF SCALAR PLUMES

Turbulent boundary layer flows continuously stir and mix embedded scalar quantities into complex structures [1]. These structures evolve in both space and time, and their characteristics vary strongly across the boundary layer, and, more weakly, in the streamwise direction. The spatial scalar structure is characterized by sparse, thin filaments of fluid with high scalar concentration (often approaching the source concentration), surrounded by larger regions of fluid with little or no scalar content. The temporal structure is characterized by relatively long periods with no scalar signal, punctuated by intense peaks with sharp temporal gradients. The spatial and temporal structural characteristics are directly linked through the mean and turbulent advective flow processes. The interception of these complex signals by physical sensors that contain intrinsic spatial and temporal averaging can change the ultimate perception of the ambient scalar structure.

A number of recent studies have detailed the hydrodynamic and scalar structure of odor plumes for a wide range of flow conditions and source geometries. Fackrell and Robins [2] used a flame ionization system to study plumes released from various heights in a wind tunnel, and Bara *et al.* [3] used a conductivity probe to study plumes over rough surfaces in a water flume. More recent studies have used planar laser-Induced fluorescence (PLIF) techniques to study dye plumes in turbulent boundary layers [4, 5]. The PLIF technique produces high-resolution, full-field quantification of the scalar structure. The acquisition of large sequences of images permits the scalar structure to be investigated from a statistical perspective.

1.2. ANTENNULE STRUCTURE AND FLICKING

In this study we focus on the design of olfactory appendages on benthic animals encountering turbulent odor plumes. Malacostracan crustaceans, such as lobsters, crabs, and mantis shrimp, have been used as model organisms for studying the behavioral algorithms used by benthic animals searching for odor sources in turbulent plumes, as well as for investigating the neurobiology of olfactory organs (reviewed in [6–9]. These crustaceans have a pair of antennules, each of which has one branch bearing an array of small hairs (called 'aesthetascs') containing chemosensory neurons (e.g., [10, 11]). The aesthetasc-bearing branches of the antennules, which function as olfactory organs (reviewed by [12–16], range from microns to centimeters in size, and differ in form from the small brush-like antennules of crabs to the long, elaborate antennules of lobsters (e.g., [11, 17]). One of the goals of our study is to explore the consequences to odor encounter of the spatial scales across which the chemical signals arriving at the receptors might be averaged by subsequent neural processing. In addition, since the fine-scale structures of an odor plume are advected past an olfactory organ, we also investigate the consequences to odor encounter of the temporal frequency responses of the neurons of antennules of various sizes and shapes.

Many crustaceans flick the aesthetasc-bearing branches of their olfactory antennules through the water. A variety of studies have focused on how such flicking enhances the penetration of odor-bearing water into the aesthetasc arrays of various species [17–24], while physical and mathematical models of flow through arrays of aesthetascs and diffusion of odor molecules have shown that water penetrates the aesthetasc array (and rates of odor-molecule encounter by aesthetascs are enhanced) during the rapid flick, but not during the slower return stroke of an antennule [17, 25–28]. Although the role of flicking in enhancing the flow of odor-bearing water through arrays of aesthetascs has been well-studied, the consequences of antennule flicking to the spatial and temporal patterns of odor encounter by olfactory antennules has only been measured for one species of lobster [24]. Another purpose of our study here is to explore how the orientation and the motion of an antennule as it flicks across the fine-scale structure of a turbulent odor plume affects the patterns of concentration arriving at the antennule.

The concentration of an odor signal above background, the onset slope of concentration arrival at the receptors, and the duration of a pulse of odor can affect the firing of olfactory neurons (e.g., [28–31]). Therefore, we quantified several biologically-relevant aspects of the scalar field as encountered by the antennules: (1) Intermittency, the percent of the time that the concentration is above defined thresholds; (2) variability, a measure of how large the fluctuations in concentration are about the mean concentration; and (3) rate of change of concentration.

2. Methodology

In order to quantify how the design and behavior of olfactory appendages affects the intermittency and variability of intercepted chemical signals, 'virtual sensors' were used to interrogate the concentration field in a dataset of a scalar plume developing in a turbulent boundary layer. A virtual sensor is a mathematical model that prescribes the location, size and shape, temporal resolution, and motion (if any) of a discrete scalar detector. A single virtual sensor spatially averages the instantaneous scalar concentrations occurring over its area. By comparing virtual sensors of different sizes, we explore the consequences of spatially averaging (e.g., by neural processing) the chemical signals arriving at the many receptors on an olfactory organ. We also specify the temporal scale over which a virtual sensor averages scalar concentrations. In addition, we use 'virtual antennules' composed of arrays of virtual sensors to study the effects of antennule flicking on scalar encounter. The scalar field as intercepted by the virtual sensor is determined by combining the mathematical model of the sensor with a high-resolution, two-dimensional scalar plume dataset. The study looks at the resulting effect of sensor design from a passive sampling perspective: the effect of the physical interaction of the sensor with the fluid (and resulting changes in the flow field) is *not* considered. The advantage of the virtual sensor approach is that it enables a number of different sensor configurations to be tested using a single plume dataset. Details of the scalar plume data and of the virtual sensor and antennule models are given in the following sections.

2.1. SCALAR PLUME DATA

A scalar plume was created within the turbulent bottom boundary layer of a laboratory water flume with a smooth bed. The freestream flow velocity was 10 cm/s. A fluorescent dye (Rhodamine 6G) was used as the scalar. Rhodamine 6G has a reported Schmidt number of $\mathrm{Sc} = 1250$ [32], which is within the range of Schmidt numbers for typical aquatic feeding signals [33]. The dye was introduced into the flow through a 1-cm hole in the upstream portion of the flume bed. The dye flow rate was minimized to produce a near momentumless (diffusive-type) release. A schematic of the flume test section, scalar source, and instrumentation is shown in Figure 1.

The spatial and temporal structure of the developing scalar plume was quantified using a planar laser-induced fluorescence (PLIF) technique. An argon-ion laser was used to excite the fluorescent dye; the resulting fluorescence was imaged with a 1024-by-1024 pixel, 12-bit digital camera fitted with a narrow band-pass optical filter that transmitted only the fluoresced wavelengths. A square area 13.6 cm on a side was imaged in a vertical plane on the centerline of the plume, resulting in images with a spatial resolution of 133 μm in the plane of the laser. The laser beam was focused such that the illumination was confined to a 280 μm out-of-plane width, which set the out-of plane spatial resolution. Computer-controlled optical scanners were used to scan the focused laser beam across the image area. A single

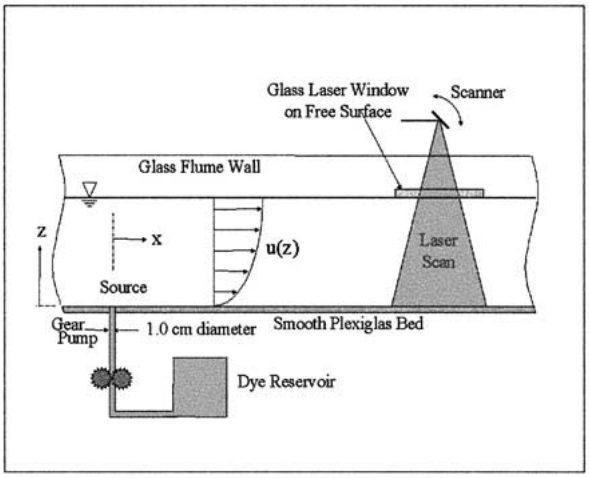

Figure 1. Side view of the flume test section showing the PLIF system.

uni-directional scan was used for each image exposure. The time to scan across the entire image was 50 ms; since the image is 1024 pixels across, the typical exposure interval for a single pixel was only 50 μs. This corresponds to a temporal resolution of 20,000 Hz, although the actual resolution was likely moderated somewhat by the response of the dye and CCD chip.

The digital images were stored real-time to a hard drive, after which they underwent post-processing for error correction. The post-processing algorithms correct the images for a number of introduced errors, including background fluorescence from the build-up of background dye in the test section, and non-uniformities in the intensity of the laser scan. Complete details of the flume, the dye source, the scalar plume, the PLIF technique, and the image post-processing algorithm are given by Crimaldi and Koseff [4]. The image dataset used for the current study consists of 5000 sequential images acquired at two frames per second in a vertical plane (aligned with the flow) on the plume centerline. The image area spans a square region covering the first 15 cm above the bed, and between 100 and 115 cm downstream of the odor source. A portion of a sample PLIF image from the sequence is shown in Figure 2.

2.2. VIRTUAL SENSORS

Virtual sensors were used to interrogate the experimentally obtained dataset of scalar plume structure. Two types of virtual sensors were used: (1) A set of simple, static sensors for investigating the effect of sensor size, shape, orientation, and temporal resolution, and (2) a biologically-inspired virtual antennule, an array of sensors used to investigate the effect of dynamic flicking. Although the geometry of the sensors can be varied within the vertical plane of the dataset, the out-of-plane (transverse) sensor dimension is set by the dataset resolution. The dataset,

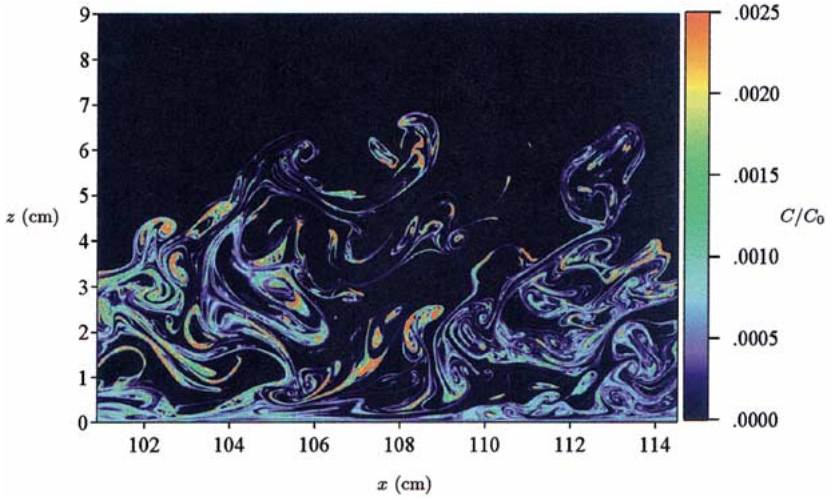

Figure 2. PLIF image showing the spatial structure of a scalar plume in a turbulent boundary layer. The streamwise distance from the source is x, and the vertical distance from the source (and the bed) is z. Concentrations are normalized by the source concentration C_0, and color-coded according to concentration strength.

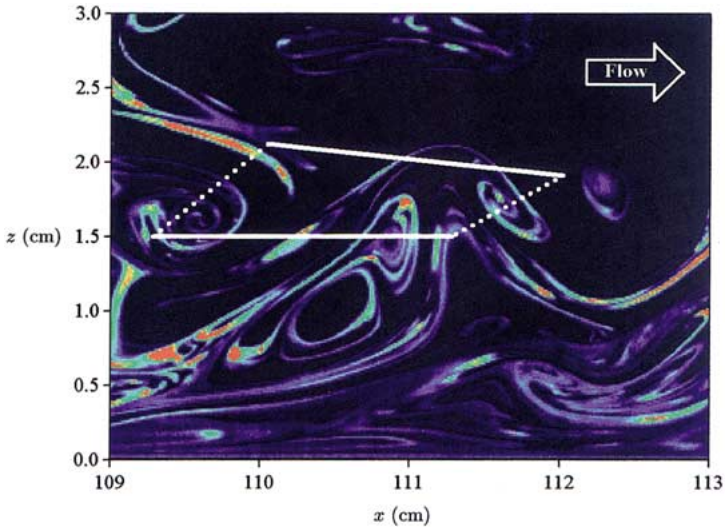

Figure 5. Range of downstroke flicking motion in an advective scalar field. The reference frame is that of an observer moving from left to right with the mean advection. Only the sensory array portion of the antennule is shown. The pivot is located at $x = 115.25$ cm, $z = 1.5$ cm.

and hence the sensors, have a fixed width (determined by the width of the focused laser beam) of 280 μm.

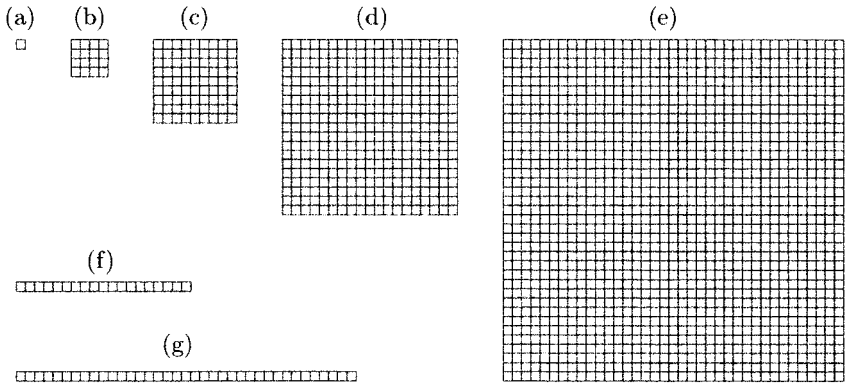

Figure 3. Diagrams of the simple virtual sensors used in the static (non-flicking) portion of the study. The internal gridding shows the scale of individual pixels within the sensor; scalar concentrations are averaged over the entire sensor. (a) S1, (b) S4, (c) S9, (d) S19, (e), S37, (f) L19, and (g) L37 [(f) and (g) shown in the $\theta = 0$ orientation].

2.2.1. *Simple Static Sensors*

We used a set of simple, static virtual sensors to investigate the effect on the intercepted scalar field of sensor size (i.e., the area over which the chemical concentrations are averaged), shape, orientation with respect to ambient water flow, and temporal resolution. Diagrams of the set of sensors are given in Figure 3. The nomenclature for the sensors consists of a shape prefix ('S' for square, 'L' for longitudinal) followed by the number of pixels (133 μm per pixel) across the primary linear dimension (denoted ℓ) of the sensor. Thus, S9 is a square sensor with 9 pixels (ℓ = 1.20 mm) on a side.

The geometry (i.e., size, shape, and orientation) of the virtual sensor determines which pixels from the dataset will be read when a concentration value is sampled. The concentrations from all of the sensor pixels are averaged to form a single value for each sample period. The temporal resolution of the sensors can also be modified as described below in Section 2.2.3.

In the present study, the virtual sensors are placed at a single location within the spatial domain of the plume dataset. This location is chosen to be consistent with the location of the biologically inspired sensor described in the next section. The center of each sensor is 2.0 cm above the bed, and 110 cm downstream from the scalar source (refer to Figure 2).

Table I summarizes some of the length scales associated with the sensors and the scalar field that they interrogate: the primary dimension of the sensor ℓ, the Batchelor scale η_B, and the scalar integral scale $\mathcal{L}_\theta$.

The smallest scalar fluctuations are set by the Batchelor scale. For weakly diffusive scalars (Schmidt number $\gg 1$), the Batchelor scale is given as [34]

$$\eta_B = \eta_K \mathrm{Sc}^{-1/2}, \tag{1}$$

Table I. Basic virtual sensor geometries.

Sensor	Pixel array	Length, ℓ (mm)	ℓ/η_B	$\mathcal{L}_\theta/\ell$
S1	1 × 1	0.133	8.3	200
S4	4 × 4	0.532	33.1	49.1
S9	9 × 9	1.20	75.0	21.7
S19	19 × 19	2.53	158	10.3
S37	37 × 37	4.92	308	5.3
L19	19 × 1	2.53	–	–
L37	37 × 1	4.92	–	–

where η_K, the Kolmogorov scale, can be estimated within the log layer at a distance z from the bed as

$$\eta_K \approx \left(\frac{\kappa z \nu^3}{u_\tau^3}\right)^{\frac{1}{4}}, \tag{2}$$

where ν is the fluid viscosity, u_τ is the boundary layer shear velocity, and $\kappa = 0.41$. For the flow used in the scalar plume dataset ($u_\tau = 0.50$ cm/s), the Batchelor scale at $z = 2$ cm is calculated to be $\eta_B = 0.016$ mm. The scalar integral scale $\mathcal{L}_\theta$ is a measure of the size of large (flux-producing) scalar structures. The scalar integral scale was calculated by integrating the scalar autocorrelation function [35]. The calculated value at $z = 2$ cm is $\mathcal{L}_\theta = 26.0$ mm.

Table I contains the ratios ℓ/η_B and $\mathcal{L}_\theta/\ell$ (for the square sensors only). These ratios compare the size of each sensor to the size range of the scalar structures the sensors are used to detect. The table indicates that the smallest sensor (S1) is 8.3 times larger than the smallest scalar scales, and that the largest sensor (S37) is 5.3 times smaller than the typical large scales in the flow.

2.2.2. *Flicking Virtual Antennule*

We used a biologically inspired sensor array, based on the olfactory antennule of the spiny lobster *Panulirus argus*, to investigate the dynamic effect of flicking on the intercepted scalar field. A schematic of the sensor array geometry is shown in Figure 4 on page 40.

The sensor array consists of 70 individual sensors in a linear arrangement that extends 2 cm from the tip of a 6-cm antennule. The width of the array is 210 μm, and each individual sensor is 286 μm long. No temporal averaging is introduced into the sensors, so they have the native temporal resolution of the dataset (f_{res} = 20,000 Hz). The antennule has a pivot point at the end opposite the sensor array, located 1.5 cm above the bed. The antennule flicks downwards 6 degrees, finishing in a horizontal orientation. As described in Section 1.2, we believe that the spiny

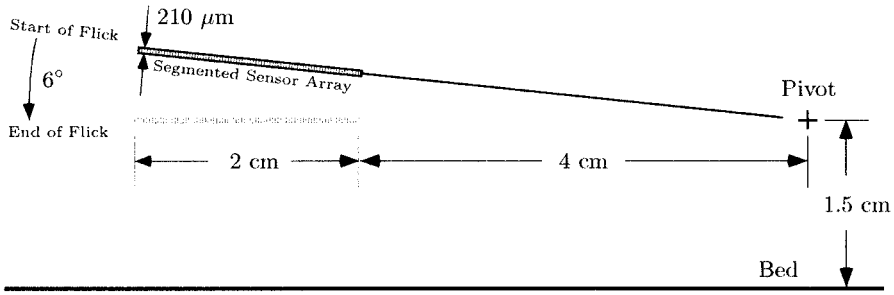

Figure 4. Virtual flicking antennule geometry (*Panulirus argus*).

lobster samples the odor field only on the downstroke portion of the flick, and we restrict the sampling of the virtual array to match this regime. The duration of the downstroke, as determined from high-speed video analysis of live animals, is 87 ms. The mean flow field in the scalar plume dataset advances approximately 7 mm during the duration of the downstroke, based on a local mean velocity of 8.2 cm/s (as measured with a laser-Doppler anemometer). By switching reference frames, the effect of advection can be approximated by moving the sensor array upstream through a single image frame during the course of the flick. This assumes that the structure of the scalar field can be 'frozen' for 87 ms. The effect of this advective scheme is shown in Figure 5 on page 40.

The 2 cm sensor array is shown before (top) and after (below) a flick through a single frame of the scalar plume dataset. The antennule pivot is initially located at $x = 115.25$ cm, $z = 1.5$ cm. During the 87 ms of the flick, the entire sensor array moves upstream (left) a distance totaling 7 mm. This movement takes place during 54 discrete time steps within the flick period, where each time step corresponds to an advective distance equal to one pixel. The area within the white lines is the region that is sampled by the array. The process is repeated for each of the 5000 images in the dataset, enabling statistical characterizations to be made concerning the effect of flicking.

2.2.3. *Temporal Resolution*

The temporal resolution of a sensor is defined as the time interval over which a sensor averages the scalar field in order to produce a single concentration reading. The temporal resolution is commonly inverted and expressed as a frequency resolution, denoted here as f_{res}. The frequency resolution of individual pixels in the scalar plume dataset is fixed at about 20,000 Hz, as described in Section 1.1. This intrinsic frequency resolution sets the upper limit of the response for virtual sensors placed within the dataset. However, the virtual sensor definitions can be designed to make the sensors behave as if they had a *slower* frequency resolution (i.e., smaller f_{res}). The technique relies on the standard 'frozen turbulence' assumption whereby the time scale associated with spatial changes in the scalar field (e.g., eddy turn-over time) is assumed to be long relative to the local advective time scale. Observation

of animated movies of the scalar field (with a 15 Hz framing rate) confirm that this is a valid assumption.

A sensor with a finite frequency resolution performs a time-based averaging process within the advecting scalar field. This effect is modeled in the virtual sensor by performing a space-based averaging process within an individual frame of the scalar field dataset. The local advection is assumed to be in the streamwise direction with a constant value equal to the local mean velocity, U (which was measured to be 8.2 cm/s using a laser-Doppler anemometer). Each pixel within a virtual sensor is then assumed to have a value equal to the average of an inclusive row of pixels upstream of the pixel in question. The number of pixels in the row to be averaged is the integer closest to $U/(f_{\text{res}}\, S)$, where S is the pixel scale (for this study, $S = 133\ \mu$m/pixel).

2.3. INTERMITTENCY ANALYSIS

When evaluating the performance of a sensor in a fluctuating scalar field, the sensitivity of the sensor must be considered. To explore the consequences of sensitivity, we calculate the percentage of time that a sensor can detect a concentration equal to or greater than a specified concentration threshold C_T (where C_T could be, for example, the detectability limit of the sensor). To be consistent with the scalar transport literature, we denote this time fraction the concentration intermittency, γ, where $\gamma = \gamma(C_T)$ and $0 \leq \gamma \leq 1$. In the current study, the intermittency is calculated based on the scalar field *as intercepted by the sensor*. Thus, the intermittency is based both on the characteristics of the scalar field and the sensor. Furthermore, the intermittency is calculated for a continuous range of threshold concentrations. For example, if $\gamma(C_T) = 0.9$, the detector registers instantaneous concentrations greater than or equal to C_T in the flow field 90% of the sampling time. As the threshold concentration C_T increases, the percentage of time that the sensor detects concentrations greater than or equal to C_T in the scalar field decreases, and thus $\gamma(C_T)$ decreases. By definition, therefore, $\gamma(C_T)$ decreases monotonically as C_T increases.

For any record of N concentration values recorded by a sensor, the intermittency can be calculated for a range of discrete concentration values [36]. First, a discrete histogram of the concentrations is formed with K bins, starting at concentration C_a and ending at C_b. Each bin then contains N_i entries, where $1 \leq i \leq K$. The discrete probability density function can then be calculated as

$$\hat{p}_i = \frac{N_i}{N} \frac{K}{C_b - C_a}. \tag{3}$$

The $\hat{p}_i$ values can be numerically integrated to form the discrete probability distribution function

$$\hat{P}_i = \frac{C_b - C_a}{K} \sum_{j=0}^{i} \hat{p}_j. \tag{4}$$

The $\hat{P}_i$ values give the probability that the sensor registers a concentration value less than or equal to the concentration of the given bin. Thus, the probability γ that the sensor registers a concentration *greater* than or equal to the stated value is given by

$$\gamma_i = 1 - \hat{P}_i \tag{5}$$

In the results that follow, the intermittency is calculated for a normalized concentration record, where the concentration is normalized by the local mean concentration, $\overline{C}$.

3. Results

The following results are grouped into two sections. First, we present results from the simple (static) virtual sensor configurations shown in Figure 3. These results focus on the effect of sensor size, shape, orientation, and temporal resolution for a stationary sensor. We then present results from the flicking virtual antennule (an array of sensors modeled after the *Panulirus argus* lobster antennule, as shown in Figure 4). The results in this second section focus on the effect of kinematic flicking for a sensor array with a single geometry and temporal resolution. For the results in both sections, the sensors are used to sample scalar concentrations from the scalar plume dataset described in Section 1.1.

3.1. RESULTS FROM SIMPLE STATIC SENSORS

The results in this section are calculated using the simple, static virtual sensors. The size, shape, and orientation of the area over which signals are averaged, and the frequency response of the virtual sensor are varied in the results presented below.

In several of the figures that follow, the intermittency γ is plotted as a function of the normalized concentration threshold $C^* = C_T/\overline{C}$, where $\overline{C}$ is the local mean concentration. *The intermittency $\gamma(C^*)$ is equivalent to the statistical probability that a sensor detects a scalar concentration equal to or larger than C^*, based on the characteristics of a particular fluctuating scalar field and on the spatial and temporal averaging of the sensor*. No minimum detectable steady-state concentration for the sensor is explicitly included into the analysis, although all real sensors have finite limits. If a sensor cannot detect steady-state concentrations less than some value of C^*, then the portion of the intermittency plots to the left of this C^* value becomes moot.

The effect of frequency resolution f_{res} (inverse temporal resolution) on intermittency is shown in Figure 6. Intermittencies calculated for sensors having four different frequency resolutions are shown in each of the two plots. Figure 6a is for a small square S1 sensor, and Figure 6b is for the larger square S37 sensor (see Figure 3 for sensor diagrams). The intermittency always decreases as C^* increases. That is, the higher the instantaneous concentration threshold, the lower the

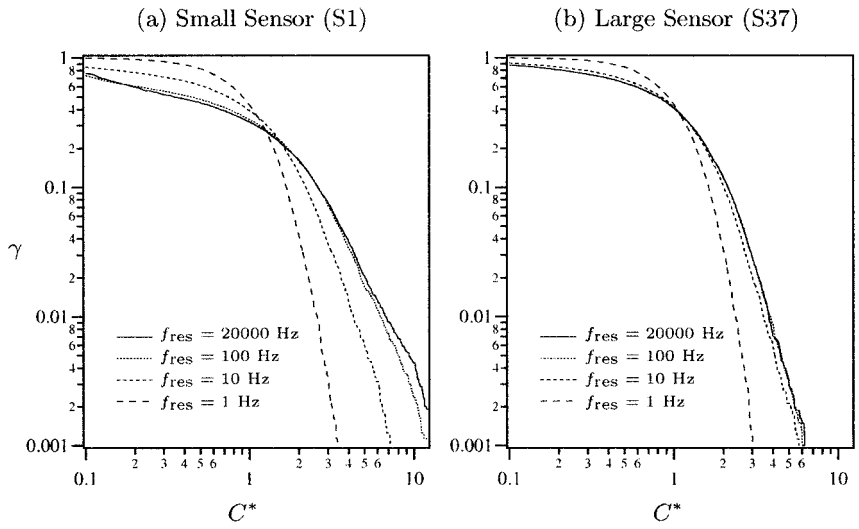

Figure 6. Effect of frequency resolution f_{res} on concentration intermittency for square sensors of two different sizes. The intermittency γ is plotted as a function of normalized concentration C^*.

likelihood of the occurrence and detection of the threshold exceedence. Figure 6a indicates, for example, that the S1 sensor with $f_{res} = 20000$ Hz frequency response would register a concentration reading greater than or equal to 3 times the mean ($C^* = 3$) 7.6% of the time ($\gamma = 0.076$) that it sampled the given flow at the given location. In other words, if the sensitivity of the sensor were such that it could only detect signals equal to or larger than $C^* = 3$, then the sensor would register the scalar field 7.6% of the time, on average.

By way of contrast, the same S1 sensor with a slower $f_{res} = 10$ Hz frequency response would register the concentrations above the same $C^* = 3$ level only 0.34% of the time (about 22 times less often than for the fast sensor). This decreased sensitivity is due to the temporal smearing of the high-concentration (but small spatial scale and thus short duration) scalar peaks. High concentrations ($C^* > 1$) are registered more frequently (γ is larger) for faster (higher f_{res}) sensor responses. The opposite is true for low concentrations ($C^* < 1$). In this study we focus on instantaneous concentrations that are higher than the local mean ($C^* > 1$) since, in natural environments, even concentrations higher than the mean are often quite weak in an absolute sense. The likelihood of detecting large concentrations decreases dramatically as the temporal response of the sensor becomes slow. On the other hand, the sensitivity of γ to f_{res} becomes increasingly small as f_{res} becomes high. Figure 6a shows that γ becomes relatively insensitive to f_{res} for values of f_{res} greater than approximately 100 Hz. Figure 6b contains the same calculations for the larger S37 sensor. The results are qualitatively the same, except that now the intermittency becomes insensitive to changes in the frequency response of the sensor at a much lower value of f_{res}. Increasing f_{res} above approximately 10 Hz

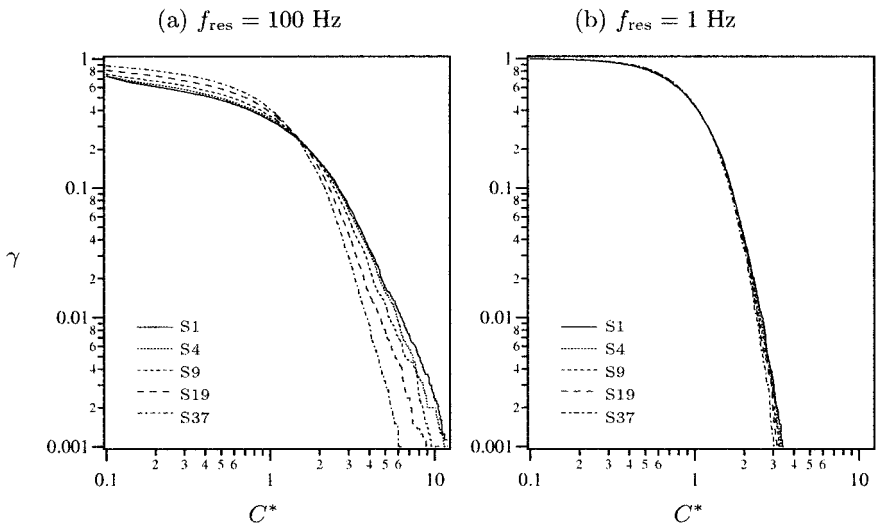

Figure 7. Effect of square sensor size on concentration intermittency for sensors with two different temporal resolutions. The intermittency γ is plotted as a function of normalized concentration C^*.

produces no change in γ because the sensitivity of the sensor to high frequency (small spatial scale) events is limited by the spatial averaging of the large sensor. The total response of the sensor, therefore, depends on the combined nature of the temporal and spatial response characteristics.

The effect of sensor size (i.e., spatial resolution) on intermittency is shown in Figure 7. The intermittencies are calculated for five different square sensors, ranging in size from the small S1 sensor to the large S37 sensor. In Figure 7a, the sensors have a frequency resolution of $f_{res} = 100$ Hz, and in Figure 7b, the sensors have a slower frequency resolution of $f_{res} = 1$ Hz. Note that increasing f_{res} above 100 Hz would not change the results in Figure 7a, as shown in the previous figure. In general, increasing the sensor size decreases the likelihood of measuring large concentrations, due to spatial averaging of high (and spatially localized) concentration peaks. For example, for the 100 Hz sensors, the value of γ at $C^* = 6$ is approximately 12 times larger for the S1 sensor as compared to the S37 sensor. In Figure 7b, the effect of sensor size is minimal, since, in this case, the sensitivity is limited by the slow 1 Hz frequency response of the sensors.

The effect of the shape and orientation of a sensor on concentration intermittency is shown in Figure 8. In Figure 8a, the intermittency is plotted for four different orientations of the L37 sensor (the highest aspect-ratio sensor). The orientation is denoted by θ, which is the angle of the sensor with respect to the bed. The position of the center of the sensor is held fixed, and the orientation is then varied. The orientation of the sensor has little effect on the resulting intermittency. Some of the observed variation is likely due to the fact that the orientation of a finite-scale sensor is being altered within a scalar field that has strong vertical gradients in the

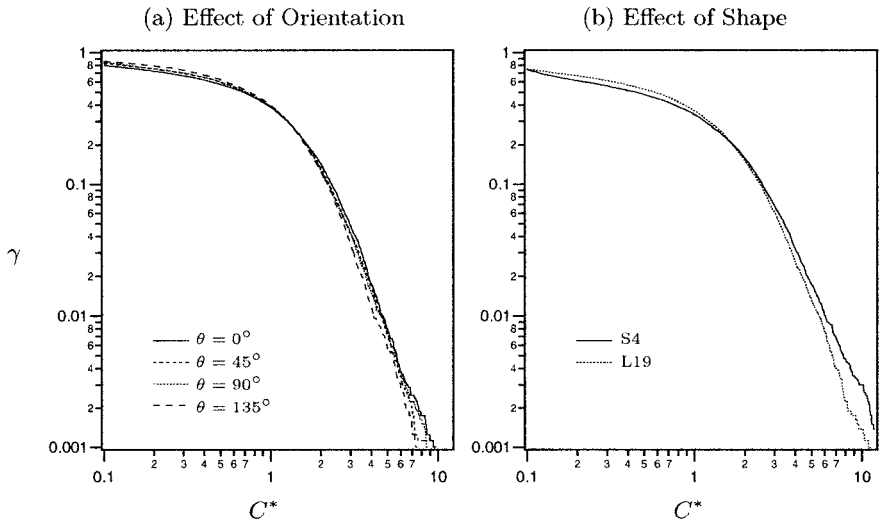

Figure 8. Effect of sensor orientation (for the L37 sensor) and shape on concentration intermittency γ.

vertical direction. The effect of shape on concentration intermittency is shown in Figure 8b. The intermittencies of the square S4 sensor and the long, thin L19 sensor are compared. These two sensors are chosen for the comparison because their areas are similar (the L19 sensor is actually 18.8% bigger than the S4). The square sensor appears to have a slightly higher intermittency (meaning better response) at high concentrations. However, some of the observed difference is consistent with the difference in area between the two sensors (compare with Figure 7a).

The effectiveness of a sensor to extract temporally varying information from complex scalar fields can be investigated by calculating the intercepted root-mean-square (rms) concentration fluctuation intensity. The rms concentration fluctuation is the simplest measure of how much of the local temporal structure of the scalar field (as opposed to the steady-state concentration) is being captured by the sensor. The virtual sensors were used to calculate the rms value of the fluctuating normalized intercepted concentration, c^*_{rms}, where the concentrations were first normalized by the local mean concentration as discussed earlier.

The sensitivity of c^*_{rms} to frequency response and sensor size is summarized in Figures 9a and 9b, respectively. In Figure 9a, c^*_{rms} is plotted as a function of f_{res} for five different sensor sizes. For all of the sensors, the amount of temporal variation detected by the signal (as quantified by c^*_{rms}) increases as f_{res} increases. Low values of f_{res} (corresponding to slower temporal resolution) result in temporal averaging of the higher-frequency components of the signal variation, leading to lower values of c^*_{rms}. As f_{res} increases, the measured value of c^*_{rms} asymptotically approaches the value that the sensor would register if there were no limitations to its frequency resolution. Note that, due to *spatial* averaging, the larger sensors (e.g. S37) quickly asymptote to a maximum c^*_{rms} value that is significantly lower than

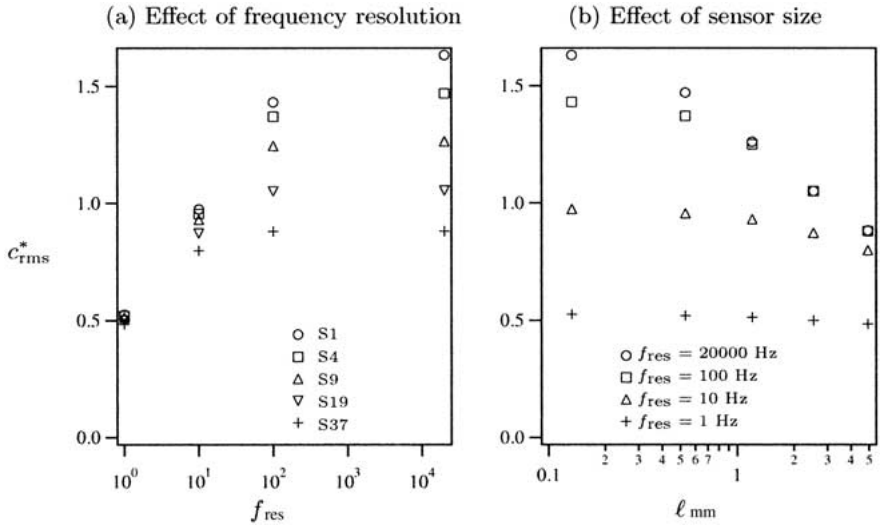

Figure 9. Effect of frequency resolution (f_{res}) and sensor size (ℓ) on rms concentration c^*_{rms}.

that obtained by the smaller sensors. The low spatial resolution of the large sensor limits the maximum possible effective frequency resolution. Figure 9b, shows the same c^*_{rms} data, now plotted as a function of sensor size ℓ. Smaller sensors are able to resolve more of the temporal fluctuation; as sensor size increases, the effect of the frequency resolution f_{res} decreases due to the limiting effect of the spatial averaging. Conversely, the sensor with f_{res} = 1 Hz, detects a c^*_{rms} value that is insensitive to sensor size, due to the limiting effect of the frequency resolution. To extract the maximum amount of temporal information content, a sensor must be both sufficiently small and fast.

3.2. RESULTS FROM FLICKING VIRTUAL ANTENNULES

The results presented in this section are calculated with the flicking virtual antennule (sensor array modeled after the *Panulirus argus* lobster antennule, as shown in Figure 4). The virtual antennule consists of a segmented, linear array of 70 discrete sensors. We investigate the effect of kinematic flicking by comparing the scalar field encountered by a flicking virtual antennule with that encountered by a static (but otherwise identical) antennule. Two different metrics of the encountered scalar field are used: Concentration intermittency and the time rate of concentration change. The concentration intermittency is calculated using the same method used in the previous section (and described in Section 2.3), except that in this section the histogram in Equation (3) is based on the *cumulative* histogram of concentrations from the 70 discrete sensors in the sensor array. In other words, the intermittency is calculated based on the intercepted concentrations from each of the 70 individual sensors in the array; the concentrations from the individual sensors are not averaged

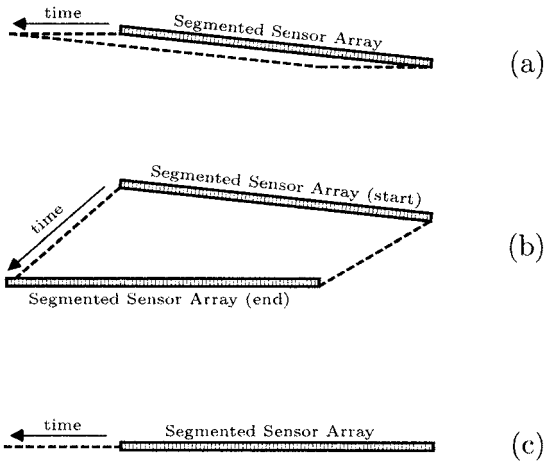

Figure 10. Effective spatial coverage over a 87 ms period for the virtual antennule in an advective scalar field. The reference frame is that of an observer moving from left to right with the mean advection: (a) Fixed antennule at the 'start' position, (b) flicking antennule (same as Figure 5), and (c) fixed antennule at the 'end' position.

into a single value (although concentrations from individual pixels within individual sensors *are* still averaged as before). The intermittency pdf's are averaged over 5000 separate 87 ms sample periods, where each sample period corresponds to a different PLIF image.

As introduced in Section 2.2.2, the effect of advection past the flicking antennule is incorporated into the analysis by switching reference frames and allowing the antennule to move upstream through individual frames of the scalar plume dataset. To determine the constituent effect of the flicking motion, a flicking antennule is compared with a static antennule. Because the flicking antennule moves through a strong vertical gradient in the scalar field statistics, there is no single static position within the flick arc than can be used for direct comparison. herefore, we evaluate the static antennule at two locations corresponding to the limiting ends of the flick stroke.

Figure 10 depicts the relative role of advection and flicking for each of the three antennule configurations (flicking, static 'start', and static 'end'). The antennules are shown in the reference frame of an observer moving from left to right with the mean advection. Figure 10a shows the first of the two static cases, this one being at the start of the flick stroke. In order to compare the static results with the flicking results, the static antennule samples each frame of the advecting scalar field for 87 ms, the duration of a flick. As time progresses, the antennule moves to the left at the local mean velocity to simulate advection. The resulting area of the scalar image that is sampled during the 87 ms period is bounded by the dashed lines. The flicking case is shown in Figure 10b. The flicking antennule arcs downward about the pivot point (not shown) over the span of 87 ms. At the same time, the antennule moves to the left to simulate advection. The sampled area is again bounded by

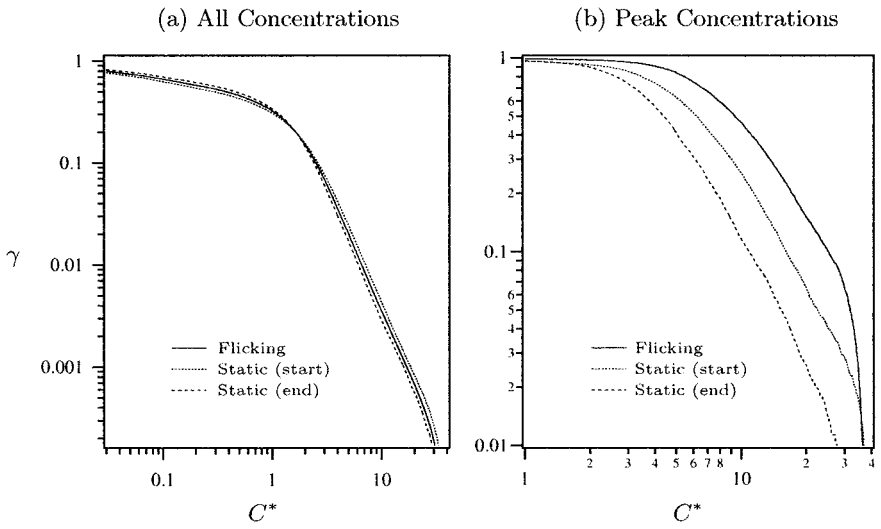

Figure 11. Effect of flicking on concentration intermittency γ as a function of normalized concentration C^*. Cumulative intermittency for all 70 sensors on the virtual antennule, calculated based on (a) all concentrations, and (b) peak concentration encountered by the antennule during each flick. The horizontal axes in the two plots have different scales.

the dashed lines. Figure 10c shows the second static case, at the end of the flick stroke. The antennule is aligned with the flow, so advection causes the antennule to sample an area that is only as high as the thickness of the antennule's sensory array (210 μm). Note that many concentration values are resampled by downstream sensors in this array configuration.

The concentration intermittency γ calculated for the ensemble (but not averaged) input from all 70 sensors in the array on the virtual antennule is shown in Figure 11a. As before, γ is calculated based on C^*, the concentration normalized by the local mean concentration. The three curves correspond to the two static cases and the flicking case. The small difference between the 'start' and 'end' static cases is attributable to the vertical gradient in the scalar structure. The mean concentration increases as distance to the bed decreases, but the near-bed *peak* concentrations are suppressed due to high mixing rates [37]. Thus, there is a higher chance of encountering large instantaneous concentrations at the 'start' location as compared to the 'end' location. Most significant is the fact that the intermittency curve calculated for the flicking case (which spans the area between the two static cases) is essentially equal to the average of the two static cases. This suggests that flicking has no effect on the statistical probability of encountering scalar concentrations of various strengths.

A different result is seen if only the *peak* intercepted concentrations are considered. For each 87 ms sample period, the peak concentration detected by any of the 70 sensors on the antennule is recorded. The process is repeated for each of the 5000 image frames and the intermittency is calculated based on this concen-

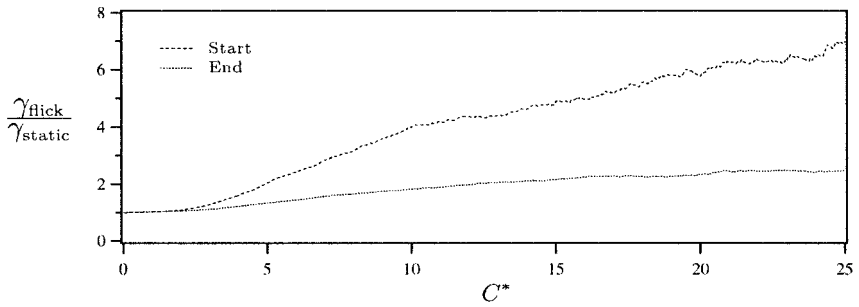

Figure 12. Ratio of intermittencies (based on peak concentrations) for the flicking case relative to the two static cases. The legend specifies the static case used to calculate the ratio. The original intermittency curves are shown in Figure 11b.

tration record. If the peak concentrations confer more information to the animal than smaller ones, then concentration intermittency based on peak concentrations is a potentially important statistic in antennule design. The calculated results for this statistic are shown in Figure 11b. Since the peak normalized concentration C^* is almost always greater than 1 (because the peak instantaneous encountered concentration exceeds the local mean), the horizontal axis has been rescaled in this plot. Intuitively, the curves in Figure 11b are elevated relative to Figure 11a, since only peak concentrations are considered. Once again, the 'start' curve lies above the 'end' curve as a result of the vertical scalar gradients in the plume. In this case, however, the flicking curve is not bounded by the static curves. Instead, the probability of intercepting a large *peak* concentration is significantly higher for the flicking case relative to either of the static cases. Since flicking enables a sensor to sample a larger spatial region of the scalar field, the peak concentration encountered by a flicking sensor is statistically larger than the peak concentration encountered by a static sensor (which encounters a smaller region of the scalar field). Thus, even though flicking does not alter the overall statistical distribution of encountered concentrations (as shown in Figure 11a), flicking does increase the magnitude of the peak encountered concentration.

The effect of flicking on encountered peak concentrations can be quantified by calculating the ratio of the flicking and non-flicking intermittency curves from Figure 11b. The resulting ratios are shown in Figure 12: The dashed line is the ratio of flicking to static 'start', and the dotted line is the ratio of flicking to static 'end'. The intermittency ratio quantifies the flicking-induced increase in the likelihood of encountering a concentration value greater than or equal to C^* during a typical sample period. Thus, Figure 12 indicates that the flicking sensor array is approximately 7 times more likely than a static sensor array at the 'start' location to encounter a concentration greater than or equal to $C^* = 25$ (25 times the local mean). The difference in the flicking-to-static ratios between the 'start' and 'end' static locations is due to vertical gradients in the scalar field. The average effect of

flicking over the full span of the flick therefore lies somewhere between the two plotted ratios.

We also investigated the effect of flicking on the perceived time rate of change of the concentration signal, $\partial C/\partial t$, arriving at the sensors on the virtual antennule. The value of $\partial C/\partial t$ at a sensor on a stationary antennule is given by the advection-diffusion equation

$$\frac{\partial C}{\partial t} = -\vec{u} \cdot \nabla C + D\nabla^2 C, \tag{6}$$

where $\vec{u}$ is the local fluid velocity past the sensor, and D is the total (turbulent plus molecular) diffusivity. The relative importance of the two terms on the right-hand side of Equation (6) is given by the Péclet number, defined as

$$\mathrm{Pe} = \frac{|\vec{u}|L}{D}, \tag{7}$$

where L is an advective length scale. When Pe is large, the diffusion term in Equation 6 can be neglected. We can then do a simple coordinate transformation to get an expression for $\partial C/\partial t$ as perceived by a *moving* sensor on a flicking antennule. For high-Pe flows, we get

$$\frac{\partial C}{\partial t} = -(\vec{u} + \vec{u}_S) \cdot \nabla C, \tag{8}$$

where $\vec{u}_S$ is the speed of the sensor measured from an inertial frame of reference. Note that, in general, $\vec{u}$ and $\vec{u}_S$ can point in different directions. If we assume that the ∇C field is statistically locally isotropic and homogeneous, then we can express the ratio of $\partial C/\partial t$ values perceived by moving and stationary sensors as

$$\frac{\frac{\partial C}{\partial t}|_{\vec{u}_S \neq 0}}{\frac{\partial C}{\partial t}|_{\vec{u}_S = 0}} = \left(\frac{|\vec{u} + \vec{u}_S|}{|\vec{u}|}\right) \nabla C. \tag{9}$$

Thus, Equation (9) predicts that concentration time derivative perceived by a moving sensor differs from that perceived by a static sensor by a factor given by the velocity ratio within the parentheses. For our study, this factor varies slightly along the length of the antennule, and with angular position during the flick. The average value (calculated halfway along the sensor array, at mid-flick) is 1.24.

We calculated $\frac{\partial C}{\partial t}$ values for all 70 of the individual sensors in the antennule array. The frozen turbulence assumption was invoked to permit calculations of time derivatives based on spatial variations in the scalar field. The resulting ensemble of concentration gradients from all 70 sensors (from 5000 individual samples of duration 87 ms) were binned into histograms. The resulting pdf's for the flicking as well as the two static cases are shown in Figure 13. The concentration gradients are normalized by the source concentration, such that $\partial \hat{C}/\partial t = C_0^{-1} \partial C/\partial t$. The pdf's show that, for all three cases, the most common value of $|\partial \hat{C}/\partial t|$ is zero, and

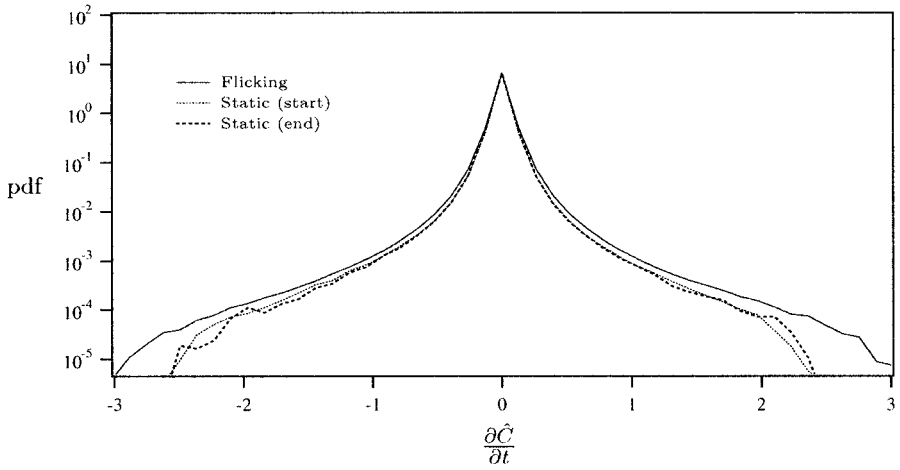

Figure 13. Cumulative pdf's of time derivative of concentration (normalized to source concentration) encountered by the 70 sensors on a virtual antennule when flicking and when static for 5000 sampling events. Positive values of the time derivative indicate onset slopes.

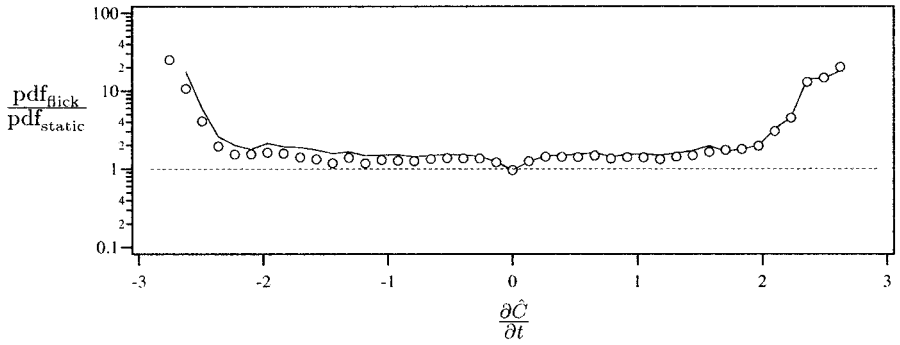

Figure 14. Ratio of flicking and static pdf's of perceived $\partial \hat{C}/\partial t$. The original pdf's are shown in Figure (13). The static 'start' case is used for calculating the ratios. The symbols represent the calculated ratio, and the solid line represents the predicted ratio based on the static case, using Equation (9) (see text).

the probability of observing larger magnitudes decreases symmetrically away from zero.

The pdf's for both of the static cases are nearly identical, but the flicking pdf indicates a significant increase in the rate of occurrence of large values of $|\partial \hat{C}/\partial t|$. The change in $\frac{\partial C}{\partial t}$ values encountered by the antennule that is caused by flicking can be quantified by taking the ratio of the flicking pdf to one of the two static pdf's (we used the 'start' case). The result is shown by the symbols in Figure 14. For $|\partial \hat{C}/\partial t| > 0$, the ratio is greater than unity (which is indicated by a dashed line), meaning that the moving antennule statistically encounters larger values of $\partial \hat{C}/\partial t$. To demonstrate that this increase in encountered $\partial \hat{C}/\partial t$ values is consistent with the increase predicted by Equation (9), we took the record of $\partial \hat{C}/\partial t$ values

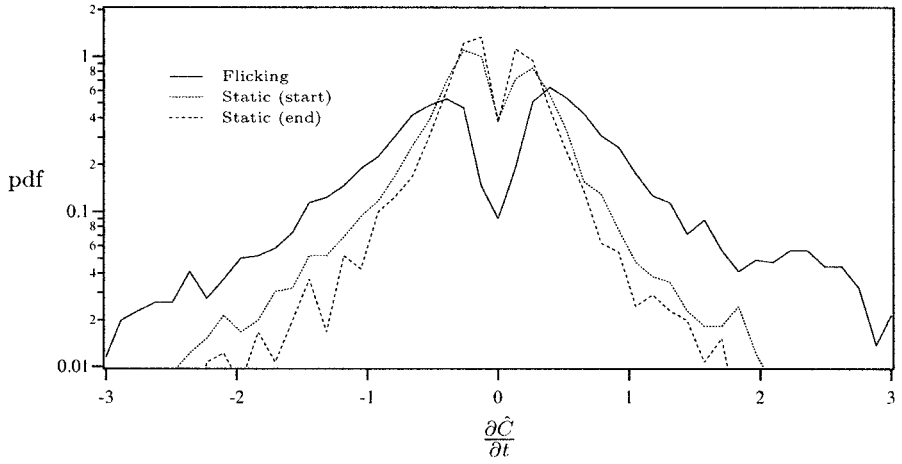

Figure 15. Cumulative pdf's of time derivative of concentration (normalized to source concentration) for the flicking and static cases, based on the peak value of the derivative measured for all 70 sensors on a virtual antennule during each of 5000 separate sample periods. Positive time derivatives indicate onset slopes.

from a static sensor and multiplied them by the velocity ratio from Equation (9) (equal to 1.24). We calculated a pdf of the resulting amplified time series from the static sensor; this pdf if shown as a solid line in Figure 14. The strong agreement between the solid line (pdf calculated based on an amplified version of the static $\partial \hat{C}/\partial t$ record) and the symbols (pdf from the flicking $\partial \hat{C}/\partial t$ record) indicates that the effect of flicking on $\partial \hat{C}/\partial t$ can be predicted using Equation (9).

Just as with the intermittency analysis, the time derivative analysis can be repeated using only the *peak* values of $\partial \hat{C}/\partial t$ encountered by any of the 70 sensors on the virtual antennule during a single 87 ms sample period. We defined the peak derivative as that with the largest magnitude, and we preserved its sign in the analysis. The pdf's of these peak values of $\partial \hat{C}/\partial t$ for 5000 separate 87 ms sample periods is shown in Figure 15. For all three cases, the pdf's are roughly symmetric, with the most common peak value of $\partial \hat{C}/\partial t$ being non-zero. Once again, the two static cases are similar, but the flicking case is markedly different. The ratio of the flicking pdf to the static 'start' pdf for the peak derivatives is shown with symbols in Figure 16.

The solid line in the figure is analogous to the solid line in Figure 14, except this time the static *peak* derivatives were amplified by a factor of 1.24 according to Equation (9) and used to form a pdf. The agreement between the predicted peak pdf (solid line) and calculated peak pdf (symbols) is qualitatively correct, but the solid line (and hence, Equation (9)) underpredicts the effects of flicking. The flicking-induced increase in the magnitude of the pdf of peak $\partial \hat{C}/\partial t$ values is in fact caused by two factors: (1) The relative motion between the sensor and the flow and (2) the increase in spatial coverage in the scalar field. Equation 9 only accounts for the first

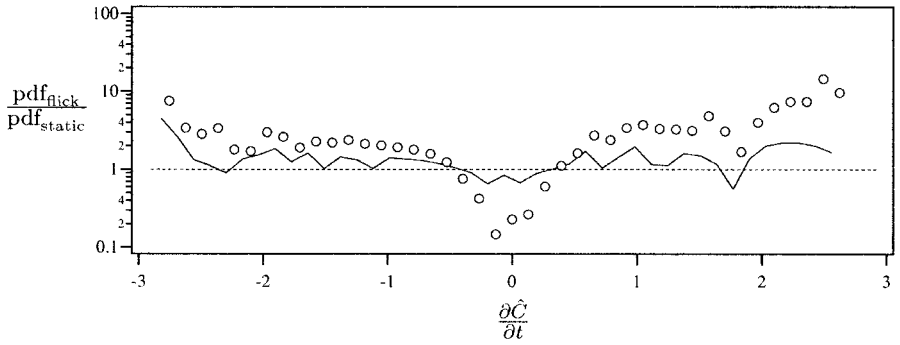

Figure 16. Ratio of flicking to static pdf's of peak values of $\partial \hat{C}/\partial t$. The original pdf's are shown in Figure 15. The static 'start' case is used for calculating the ratios. The symbols represent the calculated ratio, and the solid line represents the predicted ratio based on the static case, using Equation (9) (see text).

factor, which explains the underprediction. The significance of the results presented in Figures 11 through 16 are synthesized below in the Section 4.

In addition to changing the magnitudes of scalar concentrations and scalar derivatives encountered by an antennule, flicking also appears to change the encountered spatial structure in the scalar field. To demonstrate this, we present coherent time histories of the scalar field as encountered by the entire array of 70 sensors on the antennule during a single 87-ms sample period. This results in a space-time map of the sample, spanning the spatial extent of the sensor array on the antennule, and the time period of the sample (the duration of a flick downstroke). Representative space-time maps for the flicking and the two static cases are shown in Figure 17. Each of the three images correspond to a sample from the same image frame of the scalar plume. For clarity, the frame used here is the same frame shown in Figure 5. Figures 17a–c correspond to the cases shown in Figures 10a–c, respectively (i.e., static 'start', flicking, and static 'end'). The vertical axis in each figure is the progression of time through the 87 ms sample period, and the horizontal axis is the location along the length of the array of sensors on the antennule. Sensor 0 is closest to the pivot, and sensor 70 is at the antennule tip. The static antennules (Figures 17a and 17c) do not capture the complex spatial scalar structure that is evident for the flicking antennule (Figure 5). The diagonal banding in the figures for the stationary antennules is a result of the advection of scalar features through the space-time plane. As time progresses, a single spatial pattern of concentrations is simply shifted along the length of the antennule by the ambient flow. The flicking case shown in Figure 17b is dramatically different. The spatial scalar structure of the portion of the plume contained within the white lines in Figure 5 maps directly into the space-time map in Figure 17b of concentrations encountered by the antennule flicking through that portion of the plume. The spatial structure of the scalar field, including the scalar roll-up seen near the tip of the array, is preserved in the space-time pattern of concentrations encountered by the flicking antennule.

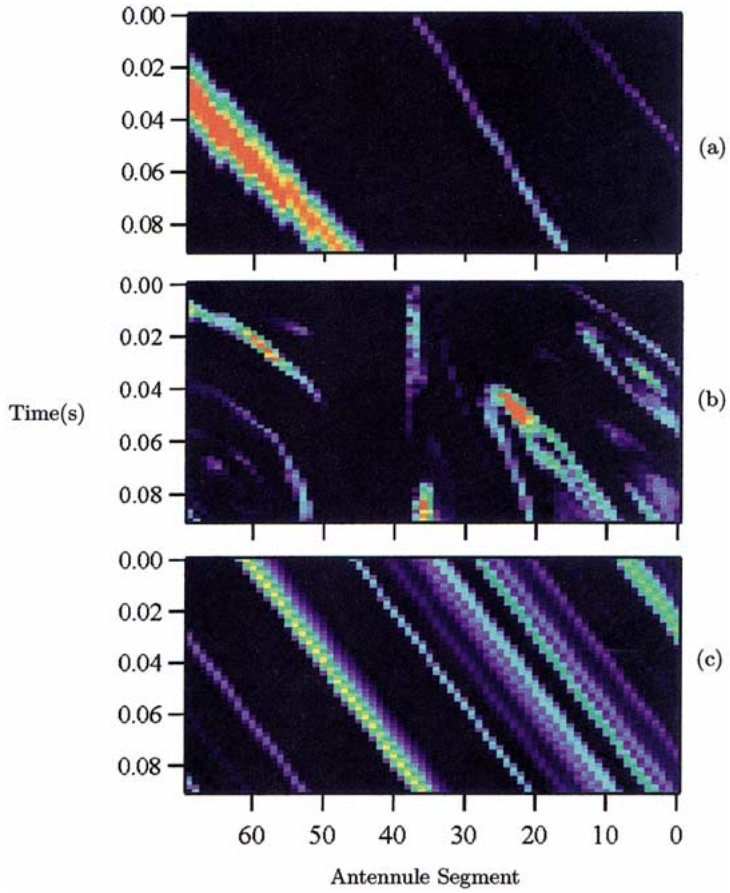

Figure 17. Space-time concentration histories at antennule sensors for three kinematic conditions for a single 87 ms sampling event: (a) Static, 'start', (b) flick downstroke, (c) static, 'end'.

These results suggest that flicking can significantly increase the scalar information content that is potentially available to the animal.

4. Discussion

We have used virtual olfactory sensors and antennules to investigate how various sampling strategies affect the intermittency and variability of intercepted chemical signals in an odor plume developing within a turbulent boundary layer. By using virtual sensors and antennules with no physical structure to interact with the flow, we have been able to separate the effects of sampling strategy (e.g., spatial and temporal scales over which odor concentrations are averaged, orientation of the antennule in the plume, and flicking) from the consequences of antennule size, morphology, and motion to the interactive shearing and mixing of the flow

and scalar field. For example, when the antennules of the spiny lobster, *Panulirus argus* flick in a turbulent plume, the fine-scale patterns of concentration in the plume penetrate into the array of chemosensory hairs on the antennule during the rapid downstroke, but this spatial pattern of concentrations in the water between the sensory hairs becomes sheared and blurred by the end of the downstroke by ambient flow along the antennule [24]. Our results in the present study, which focuses on sampling strategy rather than antennule hydrodynamics, provide insights about the consequences to chemical-signal encounter of different spatio-temporal sampling designs of olfactory organs on benthic animals and of olfactory sensors on autonomous vehicles.

4.1. FREQUENCY RESPONSE AND SPATIAL SENSITIVITY

The sensitivity of intermittency, γ, to the frequency response, f_{res}, of a sensor becomes increasingly small as f_{res} becomes large. For example, Figure 6a shows that γ becomes relatively insensitive to f_{res} for values of f_{res} greater than approximately 100 Hz. This upper limit to the effective frequency response is associated with the advective timescales of the flow (which are fast compared to the turbulent timescales). There are two advective timescales of interest: one associated with the length scale of the concentration structures, and one associated with the sensor itself. For the S1 sensor, the advective timescale for this flow (ℓ/U) is on the order of 2 ms, suggesting the potential for 500 Hz frequency response. The advective timescale associated with the scalar field itself is difficult to quantify due to the distributed nature of the scalar length scales. However, most of the scalar structures are larger than the small S1 sensor (as evidenced by the 26-mm scalar integral scale), meaning that the typical advective timescale is significantly longer than 2 ms (and significantly slower than 500 Hz). The combination of these timescale factors associated with both the sensor size and the scalar field results in a reduced effective frequency resolution on the order of 100 Hz.

The temporal and spatial scales over which the olfactory organs of animals average the chemical signals they encounter depend on the characteristics of their receptor neurons as well as on the processing of signals from those neurons by the nervous system. Chemoreceptor cells in the antennules of the lobster, *Homarus americanus*, can respond to pulses of odor lasting 50 ms, but require pulses of 200 ms or longer to measure odor concentration [29]. The neural processing of odor pulses is an active area of research (e.g., [38, 39]) and much remains to be learned about the spatial and temporal scales of odor-concentration information various animals can use. Our study of sampling strategies by antennules reveals that the spatial resolution of an antennule has an effective limit based on its temporal resolution. Our study also shows that the longer the time scale over which an animal averages chemical signals, the smaller the effect that the size of the area over which signals are averaged has on the variability of the concentration information encountered.

4.2. ANTENNA SHAPE AND ORIENTATION

The shape and orientation of a stationary olfactory organ in an odor plume might affect odor encounter in two ways: (1) Determining the area of the plume that is sampled, and (2) influencing how much the antennule disrupts and mixes the structure of the plume (e.g., [24]). Our study using virtual antennules focuses on the first of these mechanisms and shows that the shape and orientation of the sampling areas of stationary olfactory sensors make little difference to their encounters with odor filaments in turbulent plumes. However, as is discussed in the next section, the orientation of a long, slim array of sensors (as on an antennule) can have a significant impact on signal interception.

4.3. FLICKING

Flicking an olfactory antennule through the water might affect the patterns of odor concentration arriving at receptors in the aesthetascs in several ways: (1) Sweeping across a larger area of a plume than would be encountered by a stationary antennule, (2) changing the frequency content of the odor signal encountered, (3) increasing penetration of odor-bearing water into the array of aesthetascs on the antennule, and (4) altering the structure of the plume through physical interactions. Mechanism #3, the effect of flicking on water and odor movement near aesthetascs, has been demonstrated (see Introduction), and mechanism #4, the effect of flicking on physically blurring the fine-scale structures in a plume, has been measured for lobster antennules [24]. In the present study we used a virtual antennule with the size, shape, and flicking kinematics of an antennule of a spiny lobster to address mechanisms #1 and #2, the effects of flicking on the patterns of concentration in the region of a plume sampled by the antennule.

A simple argument for the statistical effect of flicking on scalar concentrations encountered by an antennule can be made as follows. For an isotropic, homogeneous scalar field, flicking and static antennules will, on average, encounter the same probabilistic distribution (pdf) of scalar concentrations, since both antennules sample portions of a common stochastic concentration field. However, the flicking antennule will, on average, encounter a larger absolute number of occurrences of all existing concentrations in a given sample period, since the flicking antennule samples a larger area (Figure 10). The trade-off is that each concentration is measured for a shorter duration. Nonetheless, the flicking antennule measures a more statistically converged snapshot of the stochastic field due to the larger sample area. Therefore, this simple argument suggests that the *peak* concentration measured by a flicking antennule will, statistically, be larger than that measured by a static antennule.

Our results support this simple argument. The scalar field used in this study was neither isotropic nor homogenous [4], but we are able to circumvent this complication by using a pair of static antennules at each limit of the flick stroke. We demonstrate that a flicking antennule encounters the same statistical distribution of

concentrations as does a stationary antennule when sampling over the same time interval (Figure 11a). However, we also demonstrate that flicking increases the magnitude of the typical peak concentration encountered during a single sweep (Figure 11b) because a flicking antennule samples a bigger area of the plume. In addition, flicking allows a long, slender olfactory organ (i.e., a one-dimensional sensor array) to encounter two-dimensional spatial structure in the concentration field in the plume (Figure 17).

The effect of flicking on the scalar gradients, $\partial C/\partial t$, encountered by antennules is due to two consequences of flicking. (1) Because a flicking antennule is moving, the speed at which structures in the plume pass across it is altered. This produces a shift in the frequency content of the scalar field encountered (statistically amplifying the magnitudes of the $\partial C/\partial t$ encountered). Since flicking and static antennules sample portions of a common stochastic derivative field, the flicking antennule should encounter the same distribution of concentration gradients as the static antennule, but the gradients should all be amplified in a statistically deterministic manner for the flicking antennule. Our results are consistent with this argument. We demonstrate that the distribution of $\partial C/\partial t$ values encountered by a flicking antennule can be predicted by amplifying the time history of the $\partial C/\partial t$ values measured by a static sensor (Figure 14). We show that the amplification depends on the ratio between flicking and advection velocities (Equation (9)). However, when we calculate the distribution of *peak* values of $\partial C/\partial t$, this amplification factor by itself underpredicts the effect of flicking (Figure 16) because flicking has another effect on plume sampling in addition to the speed of encounters with structures in the concentration field. (2) Flicking increases the area of the plume that is sampled, as described above, which enhances the encounters with *peak* quantities, thereby increasing the interception of steep onset slopes.

In this study, the flicking motion was approximately perpendicular to the mean advection. The fact that flicking increased the liklihood of encountering large peak concentrations is somewhat specific to this orientation. In particular, a flicking antennule encounters a more diverse range of odor concentrations relative to a stationary antennule when (1) the flick direction is normal to the mean advection, and (2) the flicking timescale is fast relative to the advective timescale. The relative sizes of the flicking and advection timescales also determines the extent to which the flicking antennule is able to intercept the two-dimensional spatial structure of the scalar field.

The flicking antennule in this study flicked at regular intervals that were not conditioned on the nature of the scalar structure. Animals may flick conditionally: they may, for example, be more likely to flick in the presence of high scalar concentrations or strong scalar gradients. It remains to determine the nature of this conditional flicking, and to investigate the effect it has on the characteristics of the intercepted signals.

5. Conclusions

5.1. CONCLUSIONS FROM ANALYSIS USING SIMPLE, STATIC VIRTUAL SENSORS

- In an advective environment, the spatial resolution of an olfactory sensor has an effective limit based on the temporal resolution of the sensor. For the spatial resolution range tested (signals averaged over areas of 0.017 mm^2 to 24.2 mm^2), at slow frequency responses (below 10 Hz) the spatial resolution of a sensor has almost no effect on signal intermittency or variability.
- In an advective environment, the temporal resolution of an olfactory sensor has an effective limit based on the spatial resolution of the sensor. For example, for a sensor that spatially averages signals over an area of 0.017 mm^2, there is no benefit to having a frequency resolution faster than 100 Hz (with only modest losses at 10 Hz). For sensors that average signals over larger areas, even slower frequency resolutions are adequate to capture the obtainable information.
- The orientation and shape of static sensors have very little effect on signal intermittency or variability. However, long, slender arrays of sensors (antennules) encounter smaller peak concentrations when oriented parallel to ambient flow.

5.2. CONCLUSIONS FROM ANALYSIS USING A FLICKING VIRTUAL ANTENNULE

- Flicking did not change the statistical distribution of concentration values encountered by an antennule relative to those encountered by a static antennule sampling in the same region of an advecting plume over the same period of time.
- Flicking changes the frequency content of the scalar field encountered by an antennule, thereby increasing the time derivatives (onset slopes) of concentrations encountered.
- Flicking enables an antennule to sample a larger, and thus more diverse, section of the scalar field in a given time period. Therefore, flicking resulted in an increase in the magnitude of peak encountered values of C and $\partial C/\partial t$.
- Flicking allows a one-dimensional sensor array to capture two-dimensional spatial structure in the scalar field.

Acknowledgements

This research was supported by ONR grant N0014-00-1-0794 to J. Crimaldi, ONR grants N00014-97-1-0706 and N00014-98-1-0785 to J. Koseff, and ONR grants N00014-96-1-0594 and N00014-98-1-0775 to M. Koehl.

References

1. Warhaft, Z.: 2000, Passive scalars in turbulent flows, *Annu. Rev. Fluid Mech.* **32**, 203–240.
2. Fackrell, J. and Robins, A.: 1982, Concentration fluctuations and fluxes in plumes from point sources in a turbulent boundary layer, *J. Fluid Mech.* **117**, 1–26.
3. Bara, B., Wilson, D. and Zelt, B.: 1992, Concentration fluctutation profiles from a water channel simulation of a ground-level release, *Atmos. Environ.* **26A**, 1053–1062.
4. Crimaldi, J. and Koseff, J.: 2001, High-resolution measurements of the spatial and temporal structure of a turbulent plume, *Exp. Fluids* **31**, 90–102.
5. Webster, D.R. and Weissburg, M.J.: 2001, Chemosensory guidance cues in a turbulent chemical odor plume, *Limnol. Oceanog.* **46(5)**, 1034–1047.
6. Atema, J.: 1985, Chemoreception in the sea: Adaptations of chemoreceptors and behavior to aquatic stimulus conditions, *Soc. Exp. Biol. Symp.* **39**, 387–423.
7. Atema, J.: 1996, Eddy chemotaxis and odour landscapes: Exploration of nature with animal sensors, *Biol. Bull.* **191**, 129–138.
8. Ache, B.: 1988, Integration of chemosensory information in aquatic invertebrates. In: J. Atema, R. Fay, A. Popper, and W. Tavolga (eds.), *Sensory Biology of Aquatic Animals*, pp. 387–401, Springer-Verlag, New York.
9. Weissburg, M.: 2000, The fluid dynamical context of chemosensory behavior, *Biol. Bull.* **198**, 188–202.
10. Grunert, U. and Ache, B: 1988, Ultrastructure of the aesthetasc (olfactory) sensilla of the spiny lobster Panulirus argus, *Cell Tissue Res.* **251**, 95–103.
11. Laverack, M.: 1988, The diversity of chemoreceptors. In: J. Atema, R. Fay, A. Popper, and W. Tavolga (eds.): *Sensory Biology of Aquatic Animals*. New York: Springer-Verlag, pp. 287–317.
12. Atema, J.: 1977, Functional separation of smell and taste in fish and crustacea. In: J. Le-Magnen and L. MacLeod (eds.), *Olfaction and Taste IV. Information Retrieval*, pp. 165–174, Information Retrieval, London.
13. Atema, J.: 1995, Chemical signals in the marine environment: Dispersal, detection and temporal analysis. In: T. Eisner and J. Meinwals (eds.), *Chemical Ecology: The Chemistry of Biotic Interaction*, pp. 147–159, National Academy Press, Washington D.C.
14. Gleeson, R.: 1982, Morphological and behavioral identification of the sensory structures mediating pheromone reception in the blue crab, Callinectes sapidus, *Biol. Bull.* **3163**, 162–171.
15. Hallberg, E., Johansson, K. and Elofsson, R.: 1992, The aesthetasc concept: Structural variations of putative olfactory receptor cell complexes in crustaceans, *Microsc. Res. Techn.* **22**, 336–350.
16. Atema, J. and Voigt, R.: 1995, Behavior and sensory biology. In: I. Factor (ed.), *Biology of the Lobster Homarus americanus*, pp. 313–348, Academic Press, New York.
17. Koehl, M.: 2001, Fluid dynamics of animal appendages that capture molecules: Arthropod olfactory antennae. In: *Conference Proceedings of the IMA Workshop on Computational Modeling in Biological Fluid Dynamics*.
18. Schmidt, B. and Ache, B.: 1979, Olfaction: Responses of a decapod crustacean are enhanced by flicking, *Science* **205**, 204–206.
19. Moore, P., Gerhardt, G. and Atema, J.: 1989, High resolution spatio-temporal analysis of aquatic chemical signals using microelectrochemical electrodes, *Chem. Senses* **14**, 829–840.

20. Moore, P., Atema, J. and Gerhardt, G.: 1991, Fluid dynamics and microscale chemical movement in the chemosensory appendages of the lobster, Homarus americanus, *Chem. Senses* **16**, 663–674.
21. Gleeson, R., Carr, W.E.S. and Trapido-Rosenthal, H.G.: 1993, Morphological characteristics facilitating stimulus access and removal in the olfactory organ of the spiny lobster, Panulirus argus: insight from the design, *Chem. Senses* **18**, 67–75.
22. Mead, K., Koehl, M.A.R. and O'Donnell, M.J.: 1999, Stomatopod sniffing: The scaling of chemosensory sensillae and flicking behavior with body size, *J. Exp. Mar. Biol. Ecol.* **241**, 235–261.
23. Goldman, J. and Koehl, M.A.R.: 2001, Fluid dynamic design of lobster olfactory organs: High-speed kinematic analysis of antennule flicking by Panulirus argus, *Chem. Senses* **26**, 385–398.
24. Koehl, M., Koseff, J., Crimaldi, J.P., McCay, M.G., Cooper, T., Wiley, M.B. and Moore, P.A.: 2001, Lobster sniffing: Antennule design and hydrodynamic filtering of information in an odor plume, *Science* **294**, 1948–1951.
25. Koehl, M.: 1996, Small-scale fluid dynamics of olfactory antennae, *Mar. Fresh. Behav. Physiol.* **27**, 127–141.
26. Mead, K. and Koehl, M.A.R.: 2000, Stomatopod antennule design: The asymmetry, sampling efficiency, and ontogeny of olfactory flicking, *J. Exp. Biol.* **203**, 3795–3808.
27. Koehl, M.: 2002, Transitions in function at low Reynolds number: Hair-bearing animal appendages, *Math. Meth. Appl. Sci.* (in press).
28. Stacey, M., Mead, K.S. and Koehl, M.A.R.: 2002, Molecule capture by olfactory antennules: Mantis shrimp, *J. Math. Biol.* (in press).
29. Gomez, G. and Atema, J.: 1996, Temporal resolution in olfaction: Stimulus integration time of lobster chemoreceptor cells, *J. Exp. Biol.* **199**, 1771–1779.
30. Borroni, P. and Atema, J.: 1988, Adaptation in chemoreceptor cells I: self-adapting backgrounds determine threshold and cause parallel shift of response function, *J. Compar. Physiol. A: Sens. Neural Behav. Physiol.* **164**, 67–74.
31. Borroni, P. and Atema, J.: 1989, Adaptation in chemoreceptor cells II: The effects of cross-adapting backgrounds depends on spectral tuning, *J. Compar. Physiol. A: Sens. Neural Behav. Physiol.* **165**(5), 669–678.
32. Barrett, T.: 1989, Nonintrusive optical measurements of turbulence and mixing in a stably-stratified fluid. Ph.D. Thesis, University of California, San Diego.
33. Reid, R., Prausnitz, J. and Poling, B.: 1987, *The Properties of Gases and Liquids*. McGraw-Hill, Inc., New York.
34. Batchelor, G.: 1959, Small-scale variation of convected quantities like temperature in turbulent fluid, *J. Fluid Mech.* **5**, 113–133.
35. Tennekes, H. and Lumley, J.: 1972, *A First Course in Turbulence*. The MIT Press, Cambridge.
36. Bendat, J. and Piersol, A.: 1986, *Random Data: Analysis and Measurement Procedures*, 2nd edition. John Wiley & Sons, Inc., New York.
37. Crimaldi, J.P., Wiley, M.B. and Koseff, J.R.: 2002, The relationship between mean and instantaneous structure in turbulent passive scalar plumes, *J. Turbulence* **3**(014).
38. Freidrich, R.W. and Laurent, G.: 2001, Dynamic optimization of odor representations by slow temporal patterning of mitral cell activity, *Science* **291**, 889–894.
39. Vickers, N.J., Christensen, T.A., Baker, T.C. and Hildebrand, J.G.: 2001, Odor-plume dynamics influence the brain's olfactory code, *Nature* **410**, 466–470.